ORIGINAL PAPER

Fabrication of novel magnetic chitosan/graphene-oxide/metal oxide nanocomposite beads for Cr(VI) adsorption

Chrisanne Naicker[1] · Nolwazi Nombona[2] · Werner E. van Zyl[1]

Received: 18 February 2019 / Accepted: 2 August 2019
© Institute of Chemistry, Slovak Academy of Sciences 2019

Abstract

Composites containing magnetic chitosan chloride, graphene oxide and one of three different metal oxides (MnO_2, Al_2O_3 and SiO_2) were synthesised in the morphological form of beads and applied in removing Cr(VI) species in solution. The composites were successfully characterised using IR, XRD, TGA, DSC and SEM. Adsorption studies were carried out by varying pH, concentration, temperature and time. Maximum adsorptions of 78.2, 77.8 and 75.9 mg g^{-1} for each composite bead occurred at pH 2 and at 298 K. Adsorption followed the Langmuir isotherm, with a pseudo-second-order kinetic model. Thermodynamic studies proved that adsorption occurred spontaneously with the process being exothermic. The Cr(VI) species were desorbed from the beads using NaOH and the beads could be regenerated over six cycles.

Keywords Functionalization of polymers · Adsorption · Porous materials · Recycling · Morphology

Introduction

Contamination of aquatic ecosystems has become an issue of concern due to the exponential growth of urbanisation and industrialisation (Kul and Koyuncu 2010). Heavy metal contamination in the environment poses a specific and serious threat due to bioaccumulation in aquatic organisms and accumulation in human organs. Chromium is a heavy metal present in mainly two oxidation states, Cr(III) and Cr(VI), with the latter being extremely toxic to living organisms (Costa 1997). Human health risks associated with Cr(VI) species include carcinogenic and mutagenic effects which has led to the metal being placed on the top of the priority list of toxic pollutants by the Environmental Protection Agency (EPA) (Gupta et al. 2001; Maksin et al. 2012). Chromium clean-up in aquatic systems involves the use of several techniques such as membrane filtration (Pugazhenthi et al. 2005), electrochemical precipitation (Kurniawan et al. 2006), ion exchange (Lin and Kiang 2003), reverse osmosis (Ozaki et al. 2002) and adsorption (Aragay et al. 2011; Barrera-Díaz et al. 2012). Amongst these options, the most widely applied technique showing favourable results is adsorption (Sun et al. 2014). Common adsorbents include biopolymers, metal oxides and carbon-based materials such as graphene oxide.

Biopolymers such as chitosan have also been used as adsorbents because they are biodegradable, non-toxic, economical, efficient and contain chemically active functional groups that can bind effectively to heavy metals (Wan et al. 2010). Chitosan, a chitin derivative, has the ability to effectively chelate to metal ions as a result of amino and hydroxyl groups in its framework that can form coordinate bonds with heavy metal ions in solution (Huang et al. 2009; Luo et al. 2015). Chitosan can be modified to improve its adsorption capability, biodegradability, solubility, selectivity, regeneration ability, reactivity and robustness (Rozenberg and Tenne 2008). Modifiers such as graphene oxide and metal oxide nanoparticles have been studied to improve metal adsorption capabilities of chitosan (Donadel et al. 2008; Liu et al. 2012). Graphene oxide is a hydrophilic carbon-based film which contains multiple oxygen containing functional

Electronic supplementary material The online version of this article (https://doi.org/10.1007/s11696-019-00895-7) contains supplementary material, which is available to authorized users.

✉ Nolwazi Nombona
nolwazi.nombona@up.ac.za

✉ Werner E. van Zyl
vanzylw@ukzn.ac.za

[1] School of Chemistry and Physics, University of KwaZulu-Natal, Westville Campus, Chiltern Hills, Durban 4000, South Africa

[2] Department of Chemistry, University of Pretoria, 0001 Pretoria, South Africa

groups enhancing the metal adsorption potential. The high surface area allows binding to metal oxides and the epoxy and carboxyl groups allows binding to biopolymers (Li et al. 2012).

Metal oxide nanoparticles such as iron oxide (magnetite in particular) have also been employed in forming a magnetic chitosan composite. The use of iron oxide increases adsorption capability due to fast kinetics and high surface-to-volume ratio. It also results in efficient and simple removal of the polymer from aqueous environments by the use of a magnet (Ma et al. 2007). Other metal oxides such as MnO_2, Al_2O_3 and SiO_2 are capable of efficient binding to other metals due to their high surface areas and large number of active sites available (Sharma et al. 2010; Tamura et al. 1997). The nature and characteristics of hybrid composites largely depend on morphology. Chitosan can be synthesised as beads, flakes and nanofibers. These physical characteristics affect factors such as size, porosity, surface area and dispersion of nanoparticles within the polymer which affect metal adsorption (Rozenberg and Tenne 2008). This work focuses on the incorporation of metal oxides (MnO_2, Al_2O_3 and SiO_2) onto magnetic chitosan/graphene–oxide composites for application in Cr(VI) removal from aquatic systems. Formation of hybrid composites of the above-mentioned adsorbents results in an increase in adsorption sites suited for Cr adsorption along with alteration of the physico-chemical properties as opposed to the use of individual adsorbents thus making these novel hybrid composites more suitable for the adsorption of Cr compared to individual adsorbents.

Experimental

Materials

Chemicals

Deacylated chitosan (85%), HCl (37%), concentrated H_2SO_4 (95–98%), iron oxide (magnetite, Fe_3O_4, 99.98%), methyl iodide (99%), sodium iodide (NaI), poly (vinyl pyrrolidone) (PVP), graphite flakes (99%), *N*-(3-Dimethylaminopropyl)-*N*′-ethylcarbodiimide hydrochloride (EDC, 99%), *N*-Hydroxysuccinimide (NHS, 98%), tetra-ethyl orthosilicate (TEOS), 1-methyl-2-pyrididone (99%), glutaraldehyde (25% in H_2O), α-Al_2O_3 (100–325 mesh), $MnCl_2{\cdot}4H_2O$ (99.9%), $KMnO_4$ (99.0%), H_2O_2 (35 wt %), sodium hydroxide pellets (NaOH), sodium chloride (NaCl), isopropyl alcohol and Cr(VI) standard solutions (1000 mg L^{-1}) (99.7%) were purchased from Sigma Aldrich, and used as received.

Instrumentation

Fourier transform infrared (FT-IR) spectra were recorded on a Perkin Elmer (USA) Spectrum 100 FT-IR with an ATR attachment in the wavenumber range 380–4000 cm^{-1}. Powder X-ray diffractograms (XRD) were collected on an X-ray diffractometer, Bruker AXS D8 Advance, (Germany). The scan was performed using a monochromatized X-ray beam with Cu-Kα radiation ($\lambda = 0.154$ nm). Thermogravimetric analysis (TGA) and calorimetric measurements were carried out using a TA instrument SDT-Q600 (USA). Samples were analysed under nitrogen from room temperature up to 800 °C at a flow rate of 2.5 mL min^{-1}. Field emission gun scanning electron microscopy (FEG-SEM) images were obtained on a ZEISS Ultra Plus (Germany) using an energy-dispersive X-ray (EDX) detector with Espirit 1.8.5 software. Cr(VI) analyses were carried out on a Perkin Elmer Optima 5300 DV (USA).

Synthesis

Graphene oxide Graphene oxide (GO) was prepared using a modification of Hummer's method (Hummers and Offeman 1958). Graphite flakes (5 g) were added to a cold (0 °C) concentrated H_2SO_4 (200 mL) solution under vigorous stirring in an ice bath. After dispersion of the graphite flakes, $KMnO_4$ (15 g) was added in small increments to the reaction mixture whilst maintaining the temperature below 10 °C. The mixture was stirred for 4 h and then moved from the ice bath to a water bath (35 °C) and stirred for 1 h. Deionised water (400 mL) was gradually added to the reaction mixture and stirred at 90 °C. A further volume of 1200 mL deionised water was added to the mixture followed by a 30 wt % solution of H_2O_2. The resulting suspension was rinsed with 50 mL of 5% HCl followed by washing with deionised water until the suspension reached a neutral pH. The suspension was vacuum filtered and oven dried at 60 °C overnight.

GO–MnO_2 composite GO (1.00 g) and $MnCl_2{\cdot}4H_2O$ (4.09 g) were dispersed in isopropyl alcohol (100 mL) by ultrasonication for 30 min. The slurry was heated to approximately 83 °C and stirred vigorously. $KMnO_4$ (2.27 g) was dissolved in 15 mL of deionised water and rapidly added to the boiling solution. The mixture was then refluxed for 30 min, cooled to room temperature, centrifuged, washed and oven dried at 60 °C overnight (Chen et al. 2010).

GO–Al_2O_3 composite A solution of α-Al_2O_3 (5 g) in deionised water (500 mL) was adjusted to pH 3.33 using HCl (1 M) and sonicated for 1 h. The colloid was transferred into a burette and titrated into 70 mL of GO colloid (5 mL is

1.2 mg mL^{-1}). The mixture was filtered by vacuum filtration and oven dried at 60 °C overnight (Fan et al. 2012).

GO–SiO_2 composite An alcohol:water (5:1) v/v suspension of GO (2 mg mL^{-1}) was sonicated for 3 h. The solution containing the dispersed material was added, together with 0.2 mL PVP to 40 mL of ethanol and stirred for 30 min. TEOS (0.5 mL) and ammonia (2 mL, 28% in H_2O) were added and sonicated for 30 min, then stirred at 40 °C for 12 h. The resulting suspension was centrifuged and washed and oven dried overnight at 60 °C (Lu et al. 2011).

Magnetic chitosan chloride (MCSCl) Chitosan (2 g), NaI (4.8 g), methyl iodide (11.5 mL) and a 15% NaOH solution (11 mL) were added to 1-methyl-2-pyrididone (80 mL) and refluxed at 60 °C for 1 h using ice water. The product was precipitated with ethanol, washed with ether and then re-dissolved in 1-methyl-2-pyrididone (80 mL) at 60 °C. Afterwards, NaI (4.8 g), 15% NaOH solution (11 mL) and methyl iodide (7 mL) were added with rapid stirring and the mixture was heated on a water bath at 60 °C for 30 min. An additional 2 mL of methyl iodide and 0.6 g NaOH pellets were added and the solution was stirred for 1 h. A 10% NaCl solution (40 mL) was added to the product to exchange the iodide for chloride ion followed by 3 h of stirring. The product was precipitated with ethanol, washed with ethanol and ether and dried under vacuum overnight, yielding an off-white powder. Glutaraldehyde (2 mL) was added to a solution of chitosan chloride (2 g) dissolved in acetic acid (50 mL, 20% wt) and stirred at 60° for 3 h. Fe_3O_4 (1.2 g) was added to the mixture and sonicated for a further 3 h at 60 °C. Using a syringe, the viscous solution was added dropwise into a beaker of ether to form beads. The resulting beads were oven dried at 40 °C overnight (Sieval et al. 1998).

Magnetic chitosan chloride–graphene oxide–metal oxide composites (MCSCl–GO–metal oxide) Three composites were synthesised using each of the above GO–metal oxide composites. The GO–metal oxide composites (0.1 g) were sonicated for 3 h in double-distilled water. A solution of EDC (0.05 M) and NHS (0.05 M) was added to the GO–metal oxide suspension and stirred for 2 h. The pH of the resulting solution was maintained at pH 7 using dilute NaOH. Magnetic chitosan chloride (0.1 g) was sonicated for 10 min, then mixed with the GO–metal oxide suspension and stirred at 60 °C for 2 h. The composite was washed with dilute NaOH, followed by double distilled water and oven dried at 60 °C overnight (Fan et al. 2012).

Adsorption experiments

Solutions of Cr(VI) were prepared from a stock standard solution of 1000 mg L^{-1}. Composite beads (20 mg) were placed in 50 mL solutions of 10, 50 or 100 mg L^{-1} and agitated on an orbital shaker at 100 rpm. The pH was adjusted to 2, 4, 7 and 9 at four different temperatures (20, 25, 30, 35 and 40 °C) to examine the effect of pH and temperature on adsorption capacity. At pre-determined time intervals ranging between 0 and 6 h, aliquots were removed from the solutions and analysed using ICP-OES. The amount of Cr(VI) adsorbed on the beads was determined by the following equation:

$$Q_{\exp} = \frac{\left(C_0 - C_t\right) \times V}{W},$$

where $Q_{\exp}$ (mg g^{-1}) is the adsorption capacity of Cr(VI) ion on the beads (mg Cr(VI)/g beads), C_0 (mg Cr(VI)/L) is the initial concentration (mg L^{-1}) of Cr(VI) ions, C_t (mg Cr(VI)/L) is the measured concentration of Cr(VI) ions at time *t*. V and W are the volume of solution (L) and the mass of the dry sorbent (g), respectively. For each run, five replicates were carried out, reported and compared to theoretical *Q* values.

Results and discussion

Characterisation of GO–metal oxides

Infra-red (IR) analysis

IR spectra for the composites are shown in Fig. S1. Fig S1a shows pure GO, which has a broad O–H stretching mode at 3372 cm^{-1}. Upon conjugation with MnO_2 (Fig. S1b), this broad peak (which is due to absorbed H_2O) shifted to 3204 cm^{-1}. The C=O vibration present at 1721 cm^{-1} on GO (Fig. S1a) disappeared upon conjugation, indicating that GO underwent reduction as shown in Fig. S1b to form the MnO_2 composite. The Mn–O bond was observed at 605 cm^{-1} (Han et al. 2014). Fig. S1c shows the spectrum of the GO–Al_2O_3 composite. The presence of the Al–O–Al group was confirmed by the stretch at 559 cm^{-1} (Yu et al. 2015). Fig. S1d shows the GO–SiO_2 composite, the asymmetric stretching of Si–O-Si was observed at 1045 cm^{-1} and the characteristic C–Si–O vibration band was observed 446 cm^{-1} (Yang et al. 2015; Yu et al. 2015).

Powder X-ray diffraction (XRD)

XRD diffraction patterns (Fig. S2) showed the presence of GO in the composite at $2\theta = 10.2°$ corresponding to the

(001) reflection and was present for all three composites (Chen et al. 2010; Haeri et al. 2017). The (001) reflection is predominant in GO; however, for all three composites, the reflection decreased indicating partial exfoliation of GO suggesting that the reaction of each metal oxide and GO has not reached completion. This was done on purpose to free active sites of chitosan. Metal oxide peaks were observed and corresponded to reported values (Azuaje et al. 2017; Chen et al. 2010; Haeri et al. 2017). Figure S2a shows diffraction peaks of needle-like α-MnO_2 crystals which corresponded to JCPDS 44-0141 (Jiang et al. 2011). The diffraction peaks of α-Al_2O_3 were all evident in Fig. S2b and match JCPDS 10-173 indicating that a rhombohedral crystallographic form complexed with GO (Azarmi et al. 2018). Fig. S2c clearly shows the characteristic SiO_2 (101) main peak at $2\theta = 27.2°$ which corresponds to JCPDS 79-19-12 (Shaygan et al. 2014).

TGA analysis

TGA was carried out to investigate the thermal stability of the composites (Fig. S3). For all composites (a–d) the weight loss at 100 °C was attributed to the loss of water. Weight loss of GO functional groups is shown in Fig. S3a, with weight loss in the range 100–370 °C corresponding to the decomposition of hydroxyl, epoxy and carboxylic groups (Kim and Park 2008) and weight loss in the range 450–700 °C was a result of the carbon backbone decomposition (Kou and Gao 2011).

Figure S3b shows the weight loss of GO–MnO_2. The composite exhibited three major stages of weight loss, the first stage at 219 °C and the decomposition of the oxygen-containing functional groups on the GO surface (Kim et al. 2013). The second stage between 300 and 600 °C represented the transformation of MnO_2 lattice to Mn_2O_3 which was due to the loss of oxygen-containing groups (Zhou et al. 2007). The final stage of weight loss was due to the loss of the remaining oxygen groups in Mn_2O_3 which decomposed to form Mn_3O_4 (Devaraj and Munichandraiah 2008). GO–Al_2O_3 composite (Fig. S3c) exhibited two major weight losses: the first at 211 °C which was due to the loss of oxygen containing groups, corresponding to that of GO and the other at 411 °C attributed to the decomposition of the carbon backbone (Jastrzębska et al. 2016). The GO–SiO_2 composite (Fig. S3d) showed losses at 100–200 °C and 300–465 °C. This correlates with the degradation of adsorbed silanes on the surface of GO (Palimi et al. 2014) and the decomposition of silanes grafted onto and within the GO sheets, respectively (Haeri et al. 2017).

SEM analysis

Graphene oxide showed it is composed of multiple sheets (Fig. S4a). The presence of α-MnO_2 needles on GO is clearly depicted in Fig. S4b, further confirming its crystalline nature as seen in the X-ray diffractogram. Figure S4c shows some Al_2O_3 on the GO surface, but it is mostly embedded between the GO sheets. The distinct presence of spherical SiO_2 particles coating the GO surface (Fig. S4d) indicates successful composite formation. For all composites the metal oxides are well dispersed throughout the GO sheets.

Characterisation of MCSCl/GO/metal oxide composites

Infra-red (IR) analysis

Figure 1 shows the IR spectra of the precursor magnetic chitosan chloride (MCSCl, Fig. 1a) and the three novel composites, Fig. 1b–d. The presence of the Fe–O bond at ca. 530 cm^{-1} for all composites indicates the presence of iron oxide. The successful chlorination of chitosan is shown in Fig. 1a by the peak at 1470 cm^{-1} which indicates the presence of the C–H group and shows that quarternisation has occured. The shrinkage of the peak at 1559 cm^{-1} compared to the peak on pure chitosan (Fig. S5) indicates the change of the NH_2 to N–H during the chlorination of chitosan (Mourya and Inamdar 2008). Characteristic chitosan peaks are present in all three novel composites; the peaks at 1630, 1373 and 1061 cm^{-1} indicate the presence of the amide, the CH_2–OH group of the chitosan framework and the skeletal vibration of C–O glucosamine, respectively. The C-H asymmetric stretch for chitosan was also observed at 2924 cm^{-1} (Tiwari et al. 2015). For all composites the presence of GO in the composites (Fig. 1b–d) is indicated by the broadening of the O–H band at 3380 cm^{-1} and the increase in intensity of the 1563 cm^{-1} peak due to the addition of the C=O group (Kumar and Koh 2014). The Mn–O and Al–O–Al peaks (Fig. 1b, c) are masked by the Fe–O peak, whereas the C–Si–O peak in Fig. 1d is observed at 451 cm^{-1}. The increase in intensity in the 1061 cm^{-1} peak for Fig. 1d compared to Fig. 1b and c is the Si–O-Si vibration.

TGA, DSC and SEM analysis

TGA curves of the composites shown in Fig. 2(i) exhibited a lower weight loss percentage compared to MCSCl. This implies that the addition of the GO–metal oxide composites to the beads improves thermal stability. The observed initial weight loss masses at < 200 °C are due to the loss of water, whereas weight loss between 200 °C and

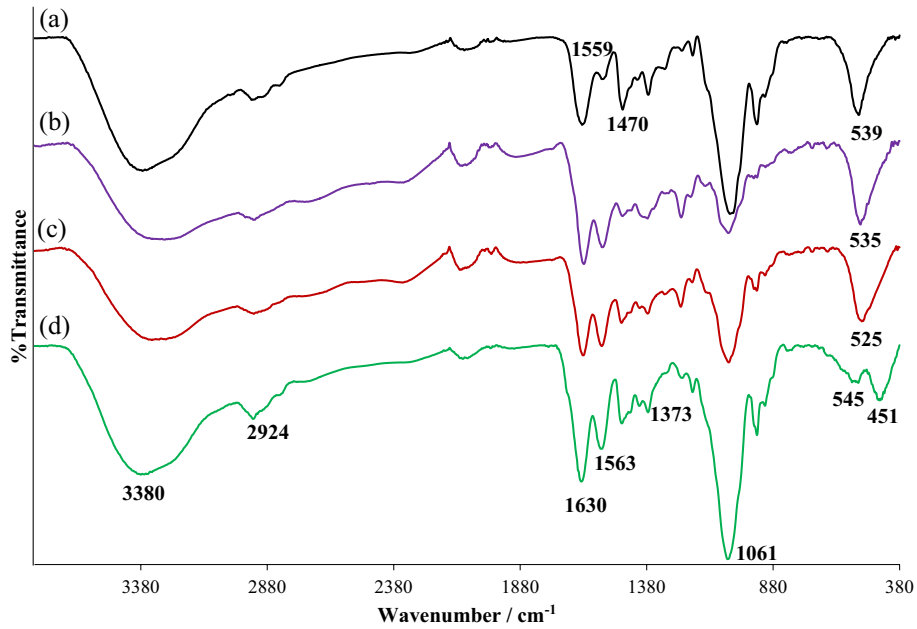

Fig. 1 FT-IR spectra of **a** MCSCl, **b** MCSCl-GO-MnO_2, **c** MCSCl-GO-Al_2O_3 and **d** MCSCl-GO-SiO_2

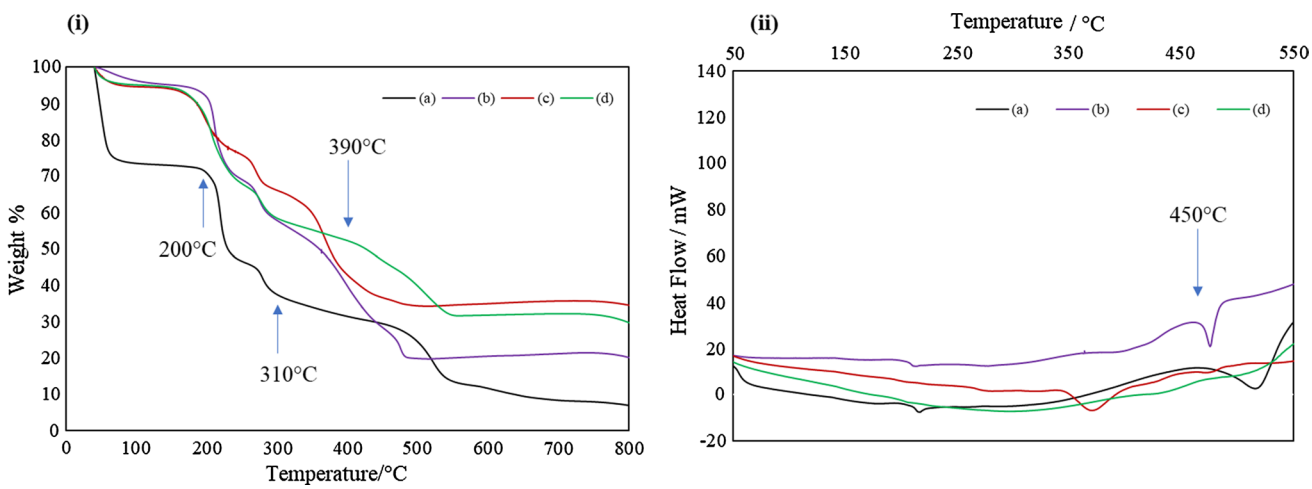

Fig. 2 (i) TGA and (ii) DSC of **a** MCSCl, **b** MCSCl-GO-MnO_2, **c** MCSCl-GO-Al_2O_3 and **d** MCSCl-GO-SiO_2

310 °C is due to the amine groups from the MCSCl backbone. Another weight loss between 310 °C and 510 °C was observed for Fig. 2a due to the loss of the quaternary groups from the MCSCl chain (Glisoni et al. 2015; Martins et al. 2013). The composites showed a similar decay (Fig. 2ib–d) from 390 °C. GO–metal oxide weight losses were masked by MCSCl degradation.

All DSC curves (Fig. 2ii) showed a common endothermic peak between 150 °C and 250 °C which correlates to the loss of water. The broad endothermic peak at 500 °C observed for MCSCl (Fig. 2ii) is caused by the reduction of the amine group on the chitosan backbone. The shift of this endothermic peak for the composites (Fig. 2iib–d) was as a result of the quaternary groups of the polymer binding to the GO–metal oxides in the composites (Glisoni et al. 2015).

SEM analysis

SEM images of the three composites are shown in Fig. 3. Figure 3a shows inner cavity of the bead, which comprises Fe_3O_4 nanoparticles and chitosan chloride. Figure 3b shows the surface of the bead which is encapsulated by the multilayers of GO and MnO_2 needles. Figure 3c is

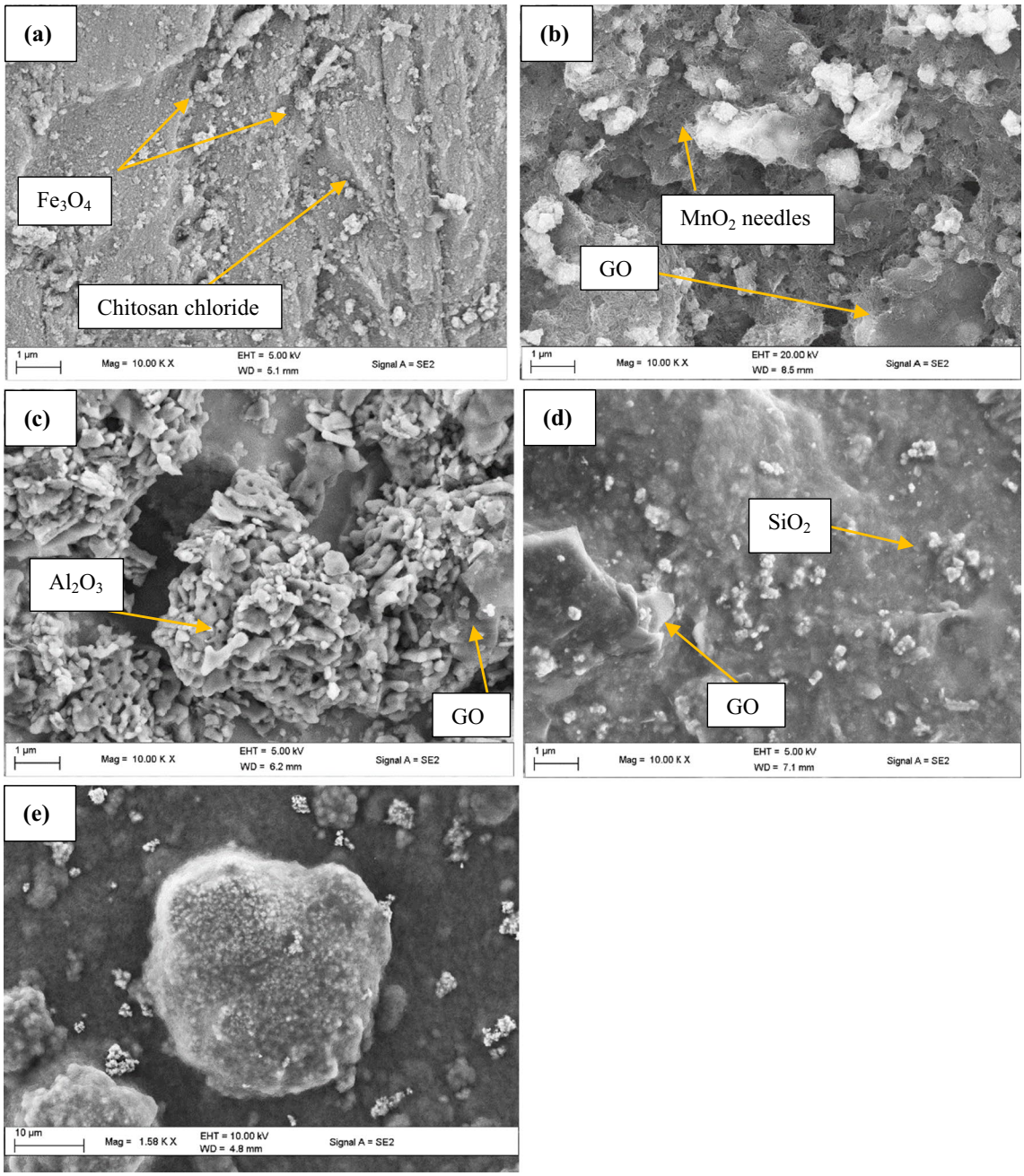

Fig. 3 SEM images of **a** Cross section of MCSCl-GO, **b** MCSCl-GO-MnO_2, **c** MCSCl-GO-Al_2O_3, **d** MCSCl-GO-SiO_2 beads and **e** top view of MCSCl-GO bead

the surface of the bead, containing flecks of GO along with Al_2O_3. Figure 3d shows the spheres corresponding to SiO_2 which are observed on the surface of the bead, along with the hazy film coating of GO surrounding the rough underlying components of MCSCl. All composites have a spherical bead shape shown in Fig. 3e.

Cr(VI) adsorption studies

Effect of pH

Determining the optimum pH used for adsorption is important because pH affects the degree of ionisation, surface

charge and speciation of the adsorbent. Chromium is known for being efficiently adsorbed by adsorbents at a low pH; however, chitosan can dissolve in acidic media (Kyzas et al. 2009). By forming a composite and incorporating metal oxides which are known to adsorb Cr(VI), the physio-chemical properties of chitosan are altered and assist in adsorption at low pH (Gheju et al. 2016). Figure S6 shows adsorption capacities tested in the pH range 2–9 in the temperature range of 20, 25, 30, 35 and 40 °C. The composites adsorbed Cr(VI) ions at each pH, with maximum adsorption occurring at pH 2 at 25 °C which proves that these parameters are optimum for Cr(VI) adsorption. pH affects the stability of chromium speciation and the surface charge of the composite (Thinh et al. 2013). Chromium exists as H_2CrO_4 at pH 1; however, the species changes within the range of pH 1–6 and forms species such as $Cr_2O_7^{2-}$, $Cr_3O_{10}^{2-}$ and predominantly $HCrO_4^-$. The $HCrO_4^-$ species exist mainly at pH < 4 and is strongly attracted to the positive quaternary amine groups in the magnetic chitosan composites which result in a positive surface charge. Adsorption is also increased by the electrostatic interaction between the composite (Karthikeyan et al. 2005). Notably, adsorption at pH 9 was higher than the common chitosan-based composites indicating that the physiochemical properties of the composites enhanced adsorption capability (Elwakeel 2009). The addition of metal oxides plays a role in increased uptake for instance, in alkaline media; the electrostatic and chemical interactions favour adsorption of CrO_4^{2-}, whereas in acidic media the surface charge of the metal oxides are positive which attract $HCrO_4^-$ ions (Du et al. 2015; Ge et al. 2013). The higher uptake value at pH 9 may be related to the presence of the trimethylammonium chloride which acts as an ion exchanger in basic media. The following mechanisms of interaction with Cr(VI) at acidic and basic media are as follows:

(a) Acidic media

$$RNH_2^+Cl^- + HCrO^{4-} \leftrightarrow RNH_2 + HCrO^{4-} + Cl^-$$

$$R-N^+(CH_3)_3Cl^- + HCrO^{4-} \leftrightarrow R-N+(CH_3)_3HCrO^{4-} + Cl^-$$

(b) Basic media

$$2R-N+(CH_3)_3Cl^- + Cr_2O_7^{2-} \leftrightarrow (2R-N+(CH_3)_3)Cr_2O_7^{2-} + 2Cl$$

$$R-N^+(CH_3)_3Cl^- + CrO_4^{2-} \leftrightarrow (2R-N+(CH_3)_3)CrO_4^{2-} + Cl^-$$

This suggests that the incorporation of metal oxides and chlorination of chitosan improves the stability and adsorption capacity of the chitosan-based composite. The decrease in Cr(VI) adsorption at pH 4 and pH 7 may have been due to a decrease of $HCrO_4^-$ ions.

Effect of contact time

The effect of Cr(VI) adsorption on the beads was monitored over a period of 6 h at three concentrations (10, 50 and 100 mg L^{-1}). The range of concentrations was chosen to determine the maximum adsorption capacity. Concentration range was capped at 100 mg L^{-1} due to previous studies on individual adsorbents which show a decrease in adsorption percentage at concentrations higher than 100 mg L^{-1}. Figure 4 shows that the amount of Cr(VI) ions adsorbed on the composites increased (for all concentrations) over time until adsorption equilibrium was reached, which was between 2 and 3 h of the total experiment time of 6 h. The beads showed the adsorb Cr(VI) with high efficiency at the lowest concentration with maximum adsorption occurring after ca. 2 h. However, at the highest concentration maximum

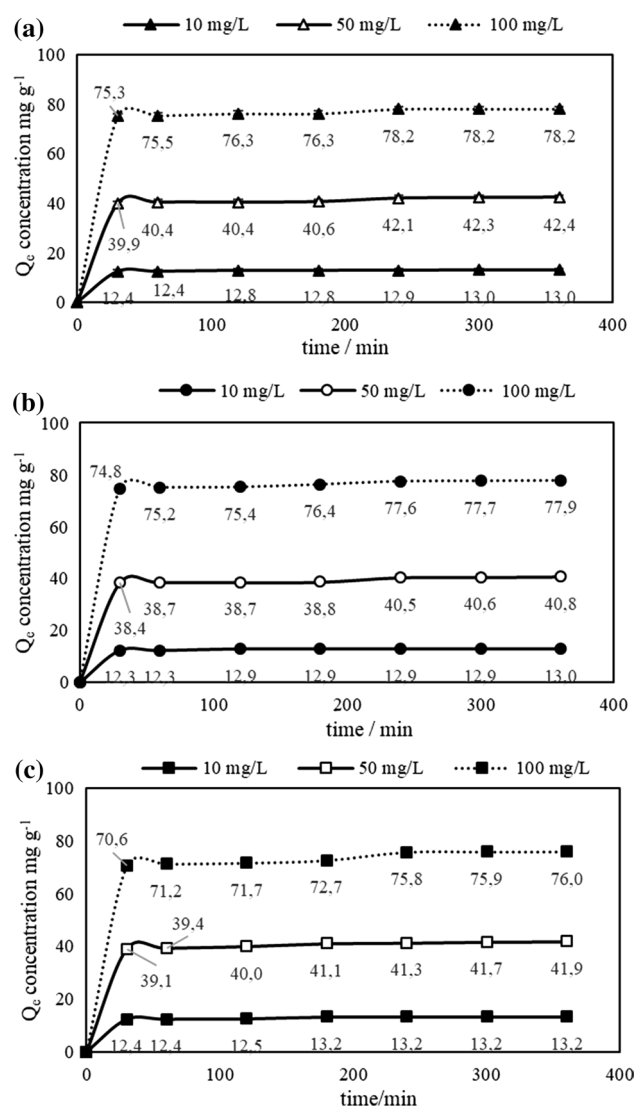

Fig. 4 Effect of contact time on Cr(VI) uptake at pH 2, 298 K for **a** MCSCl-GO-MnO_2, **b** MCSCl-GO-Al_2O_3 and **c** MCSCl-GO-SiO_2

adsorption occurred after 3 h. The difference in adsorption time indicated that the 100 mg L^{-1} solution is the most effective for Cr(VI) adsorption. In the case of adsorption efficiency (fastest Cr(VI) adsorption time to equilibrium) vs adsorption capacity (maximum concentration of Cr(VI) adsorbed), the adsorption capacity is favoured for this study because maximum concentration is reached after a relatively short period of time.

Adsorption isotherm

Adsorption isotherms are essential in determining the efficacy of the adsorption process. The experimental data of Cr(VI) adsorbed on the beads at pH 2 and 25 °C at the initial Cr(VI) concentration of 100 mg L^{-1} were used to determine the adsorption equilibrium between the metal and Cr(VI) ions in solution at equilibrium, by fitting it with the Langmuir and Freundlich isotherms. Fig. S7 shows the Langmuir isotherms of the composites expressed according to Eq. (1):

$$\frac{C_e}{q_{\exp}} = \frac{1}{q_{\max}} C_e + \frac{1}{q_{\max} K_L}, \tag{1}$$

where C_e is the equilibrium concentration (mg L^{-1}), $q_{\exp}$ the amount of metal ion (mg g^{-1}) sorbed, $q_{\max}$ is the theoretical binding capacity for monolayer adsorption (mg g^{-1}) and K_L is binding affinity constant (L mg^{-1}). The values of $q_{\max}$ and K_L are shown in Table 1.

The theoretical adsorption capacities ($q_{\max}$) from the Langmuir plot were all slightly higher than the experimental values obtained (Table 1), but within the standard deviation range. However, compared to previous Cr(VI) studies involving magnetic chitosan, graphene oxide and metal oxides, all three synthesised composites had a higher adsorption capacity (Table 2). Adsorption capacity of MCSCl–GO–MnO_2 is 94-fold higher than the maximum adsorption capacity of MnO_2, while MCSCl–GO–Al_2O_3 is 13.6-fold higher than γ-Al_2O_3 and MCSCl–GO–SiO_2 is sevenfold larger than thiophene-supported SiO_2. When compared to magnetic chitosan, adsorption capacity increased in the range of 24.1–26.4 mg g^{-1} and 43.5–45.8 mg g^{-1} for graphene oxide composites. The difference in results indicate that chitosan and graphene oxide contain a majority of the adsorption sites, while the metal oxides serve to further enhance adsorption capacity. The binding affinity constant (K_L) gives an indication of the magnitude of affinity between the adsorbent and adsorbate molecules. The value of K_L decreased in the following order MCSCl–GO–MnO_2 > MCSCl–GO–SiO_2 > MCSCl–GO–Al_2O_3. This suggests that Cr(VI) adsorption is favoured on MCSCl–GO–MnO_2 compared to the other two composites, which correlates to it having the highest adsorption capacity. MCSCl–GO–SiO_2 has the second highest K_L value; however, it has a lower adsorption capacity compared to MCSCl–GO–Al_2O_3. This may be due to more favourable electrostatic interactions between Al_2O_3 and Cr(VI) in solution at pH 2.

The Freundlich isotherm is expressed by Eq. (2):

$$\ln q_{\exp} = \frac{1}{n} \ln C_e + \ln K_F \tag{2}$$

Table 2 Studies of Cr(VI) using various adsorbents

Composite	Adsorption capacity Cr(VI) mg g^{-1}
MCSCl-GO-MnO_2*	78.2
MCSCl-GO-Al_2O_3*	77.8
MCSCl-GO-SiO_2*	75.9
EDTA cross-linked magnetic chitosan (Hu et al. 2011)	51.8
Magnetic graphene nanocomposites (Zhu et al. 2012)	1.03
CTAB modified graphene (Wu et al. 2013)	21.57
Porous Fe_3O_4 hollow microspheres/graphene oxide composite (Liu et al. 2013)	32.33
MnO_2 (Gheju et al. 2016)	0.83
γ-Al_2O_3 (Ge et al. 2013)	5.7
Thiophene supported SiO_2 (Jodeh 2016)	10.62

*This study

Table 1 Isotherm and kinetic parameters for Cr(VI) adsorption onto composite beads

	Intraparticle diffusion		Langmuir				Freundlich	Pseudo-first-order	Pseudo-second-order
	k_i (mg g^{-1} $min^{1/2}$)	C (mg g^{-1})	R^2	$q_{\exp}$ (mg g^{-1})	$q_{\max}$ (mg g^{-1})	K_L (mol L^{-1})	R^2	R^2	R^2
MCSCl-MnO_2	0.1424	74.5	0.9999	78.2	93.4	0.090	0.9876	0.9108	1
MCSCl-Al_2O_3	0.1834	73.7	0.9956	77.8	86.9	0.082	0.9881	0.9406	1
MCSCl-SiO_2	0.2502	69.2	0.9999	75.9	81.3	0.087	0.9902	0.9202	1

where q_{exp} (mg g^{-1}) and C_e (mg L^{-1}) are the adsorbed and liquid-phase Cr(VI) concentrations at equilibrium, K_F is the adsorption capacity constant and n the intensity constant. $1/n$ gives an indication of the adsorption intensity and K_F the adsorption capacity. Fig. S7 shows the isotherm plots. The Freundlich isotherm gives an indication of whether adsorption occurs by stacking of metal ions on adsorption sites. The Langmuir isotherms had R^2 values > 0.99 which was larger than the R^2 values of the Freundlich isotherms, indicating that adsorption for the composites favour monolayer adsorption.

Adsorption kinetics

Pseudo-first-order and pseudo-second-order kinetic studies

The adsorption kinetic studies of the composites were studied to determine type of adsorption and the rate-limiting step. The pseudo-first-order kinetics as expressed by Eq. (3) is an indication of whether adsorption occurs by physisorption.

$$\log\left(q_e - q_t\right) = \log q_e - \frac{k_1}{2.303}t, \tag{3}$$

where k_1 is the rate constant (min^{-1}), q_e is the concentration of Cr(VI) ions adsorbed at equilibrium (mg g^{-1}) and q_t is the concentration of Cr(VI) ions adsorbed at time t (mg g^{-1}) (Fig. S8).

The pseudo-second-order kinetic model was used to determine the rate-limiting step by Eq. (4). This model favours chemisorption as the rate-limiting step.

$$\frac{t}{q_t} = \frac{1}{k_2 q_e^2} + \frac{t}{q_e} \tag{4}$$

A linear plot of t/q_t vs t determines the rate constant k_2 (g mg^{-1} min^{-1}) and q_e the equilibrium adsorption capacity (mg g^{-1}). The linear plots of the pseudo-first-order and pseudo-second-order models are shown in Fig. S8 and the calculated correlation coefficients are shown in Table 1. The pseudo-second-order R^2 for the composites are larger than the pseudo-first-order model, indicating a better fit of linearity. This implies that the rate-limiting step of adsorption is chemisorption. Chemisorption involves the sharing and/or exchange of electrons between composite and Cr(VI) ions using valence forces. The chitosan in the composite contains protonated amine groups which are attracted to negatively charged Cr ions which results in chemisorption as the favoured rate-limiting step (Lee et al. 2009).

Intra-particle diffusion model

The intra-particle diffusion model was considered in order to gain better insight into the sorption mechanism. The sorption process can occur in four steps: (a) external mass transfer of the metal ions in solution to the boundary/film layer, (b) movement of metal ions from boundary film layer to the surface of adsorbent, (c) diffusion from the surface of the sorbent particle to adsorption sites and (d) metal ion complexation, sorption or precipitation at sorption sites (Palimi et al. 2014). Investigation into steps (a) and (b) were eliminated by agitating the solution throughout the adsorption process, and step (d) was eliminated because adsorption was rapid and Cr(VI) composite interactions did not lead to precipitation. These eliminations resulted in sorption to be a quasi-instantaneous process, which lead to an investigation of the boundary/film layer and intra-particle diffusion mechanism (Weber and Morris 1962). The proposed adsorption rate processes (Pugazhenthi et al. 2005) are expressed in Eq. (5):

$$q_t = k_i.t^{0.5}, \tag{5}$$

where q_t is the concentration of the solute within the solid and k_i is the intraparticle diffusion rate constant. A linear plot of q_t vs $t^{0.5}$ indicates that the adsorption rate is controlled by particle diffusion. If not linear then the rate is controlled by boundary/film layer sorption (Mckay et al. 1986). Figure S9 shows that the process of sorption for the composites is based on two phases as indicated by the two different linear fits. This implies that the intra particle diffusion is not the

Table 3 Thermodynamics parameters of Cr(VI) adsorption onto composite beads

MCSCl-MnO_2				MCSCl-Al_2O_3			MCSCl-SiO_2		
Temp. (K)	ΔH° kJ/mol	ΔS° J/mol	ΔG° kJ/mol	ΔH° kJ/mol	ΔS° J/mol	ΔG° kJ/mol	ΔH° kJ/mol	ΔS° J/mol	ΔG° kJ/mol
293	−26.34	51.43	−41.41	−8.84	6.99	−10.89	−22.92	39.87	−34.60
298			−41.66			−10.92			−34.80
303			−41.92			−10.96			−35.00
308			−42.18			−10.99			−35.20
313			−42.43			−11.03			−35.39

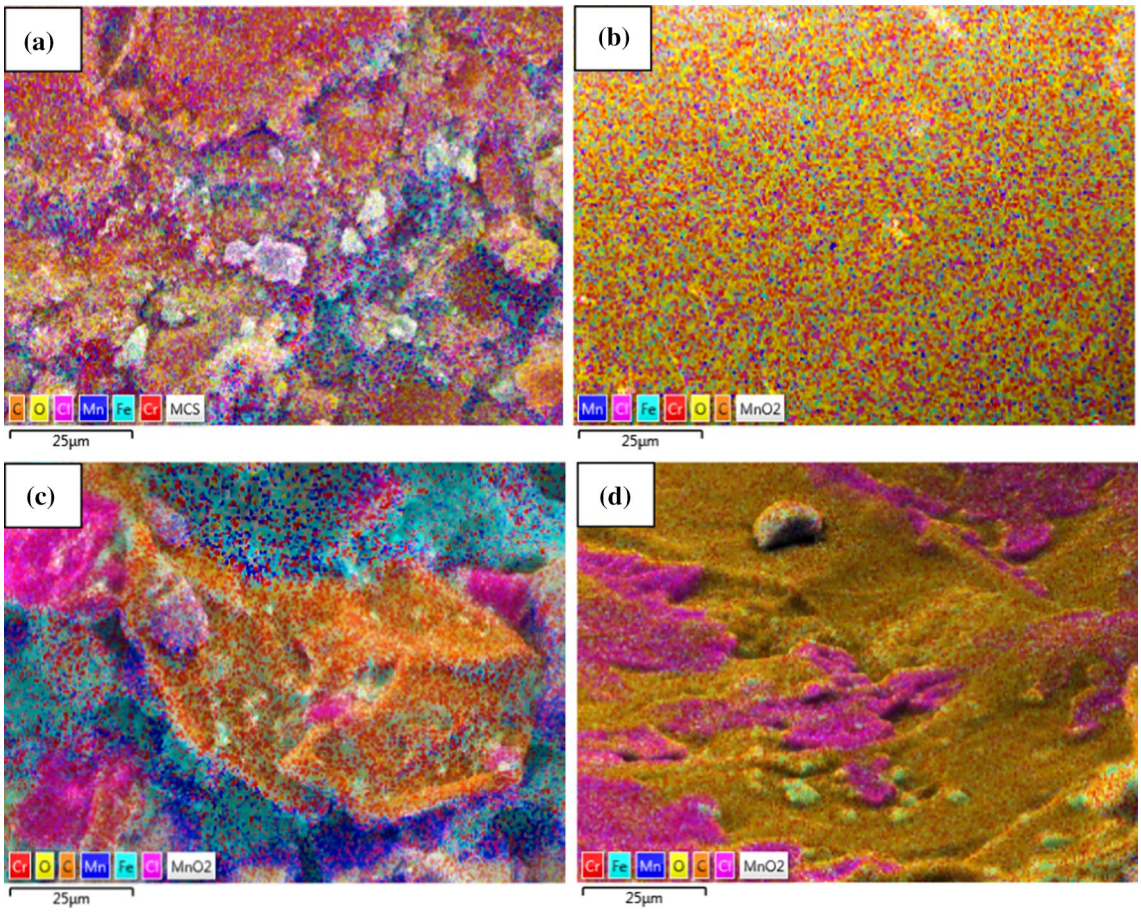

Fig. 5 SEM-EDX images of **a** Cr(VI) adsorbed surface, **b** Cr(VI) adsorbed cross-section, **c** Cr(VI) desorbed surface and **d** Cr(VI) desorbed cross-section MCSCl-GO-MnO_2 bead

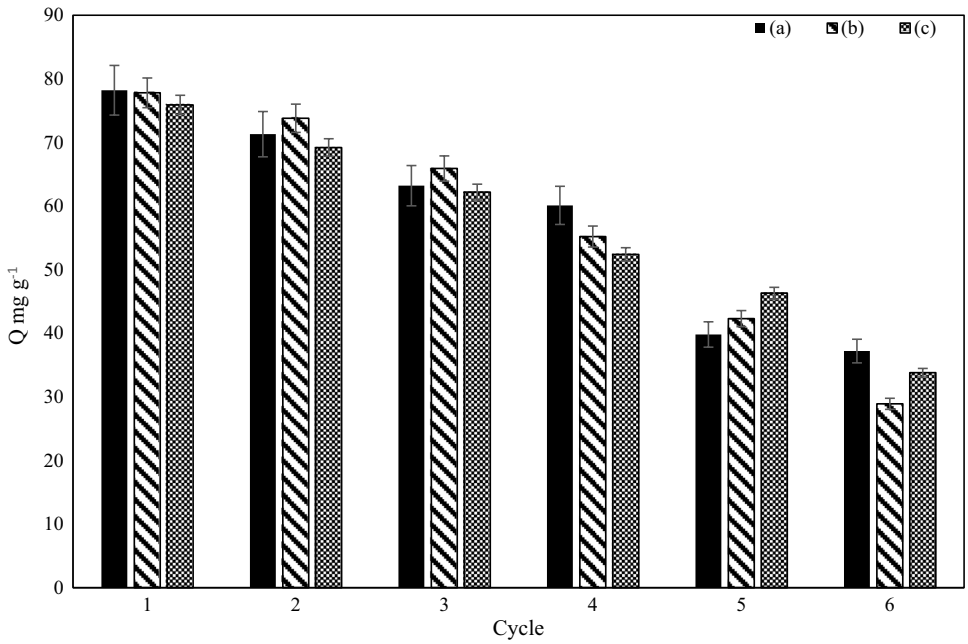

Fig. 6 Adsorption–desorption capacity of Cr(VI) ions onto **a** MCSCl-GO-MnO_2, **b** MCSCl-GO-Al_2O_3 and c MCSCl-GO-SiO_2

rate-limiting step for the entire adsorption process (transport of Cr(VI) ions from the solution to the surface of the adsorbents). Multi-phase steps are commonly present with porous adsorbents. The initial linear plots indicate that boundary/film layer is responsible for sorption, whilst the latter plot is due to intraparticle diffusion, i.e., porous adsorbents have high k_i, values and high C values are an indication that the sorption process favours boundary layer sorption (Mckay et al. 1986). The MCSCl–GO–SiO_2 composite had the highest k_i value and is, therefore, the most porous and favours intraparticle diffusion compared to MCSCl–GO–MnO_2 which favours boundary/film layer sorption (Table 1). Sorption and porosity characteristics are dependent on the type of metal oxide in the composite. MnO_2 and Al_2O_3 have been previously reported to favour boundary/film layer adsorption due to its lack of porosity (Belgin Ergül and Mehmet 2014), and SiO_2 is known to favour intraparticle diffusion because it is highly porous but its composites with SiO_2 do not have the highest adsorption capacity, which suggest that porosity of the bead is not the most important factor in the adsorption process (Sekine and Nakatani 2002).

Thermodynamic studies

The thermodynamic characteristics of the adsorption process were investigated to determine the effect of temperature on adsorption using van't Hoff equation (Fig. S10) (6):

$$\ln K_L = -\frac{\Delta H^\circ}{RT} + \frac{\Delta S^\circ}{R}, \tag{6}$$

where ΔH° is the change in enthalpy, ΔS° is the change in entropy, R is the universal gas constant (8.314 J mol^{-1} K^{-1}) and T is the absolute temperature (Kelvin). The ΔH° and ΔS° values were calculated for each composite and are shown in Table 3. ΔH° is negative for all three composites which indicates the adsorption process is exothermic, whereas the positive ΔS° values indicate randomness during Cr(VI) adsorption. MCSCl–GO–MnO_2 and MCSCl–GO–SiO_2 had larger ΔS° values compared to MCSCl–GO–Al_2O_3; this difference implies that larger ΔS° results in larger degrees of freedom at the solid–liquid interface during Cr(VI) adsorption which causes structural changes to the adsorbent and can influence the rate of adsorption (Li et al. 2012). Additionally, the Gibbs free energy (ΔG°) was calculated and the same trend as ΔS° was observed, indicating that adsorption is favoured and occurred more rapidly on the MCSCl–GO–MnO_2 and MCSCl–GO–SiO_2 composite compared to the MCSCl–GO–Al_2O_3 composite. The trends of ΔS° and ΔG° are the same as the calculated K_L values in Table 1. This proves that the thermodynamic parameters influence the binding affinity of all three composites.

Desorption and regeneration

In order for an adsorbent to be economically feasible it must be recyclable. The Cr(VI) ions were removed from the beads by soaking them in a conc. NaOH solution for 24 h. The concentrated alkaline medium was able to alter the surface charge of the composites, thus weakening the electrostatic interaction between the composite and metal ion and thereby promoting desorption. EDX images of adsorbed and desorbed MCSCl–GO–MnO_2 beads are shown in Fig. 5. Images for the other composites are present in Fig. S11. Figure 5a shows the surface of the bead after adsorption and Fig. 5b shows the cross-section clearly depicting that adsorption occurred throughout the inner sections of the bead and not only on the surface, confirming the porosity of the beads facilitate adsorption of Cr(VI). Figure 5c–d shows the successful desorption of Cr(VI) from the surface and inner cavity of the bead. The mass balance for the adsorption and desorption process was analysed by ICP-OES for each cycle. Figure 6 shows the adsorption–desorption cycles of the composites, and the percentage of adsorbed Cr(VI) for composite (a), (b) and (c) decreased to 47.5, 37.1 and 44.5%, respectively, after six cycles. This decrease suggests that composite (a) has stronger physio-chemical properties (GO–MnO_2 is formed by covalent bonding) compared to (b) and (c), with the Al_2O_3–GO bond being the easiest to dissociate. The decrease in % adsorbed of the composites also correlates to the binding affinity (K_L), which indicates that the physio-chemical properties of the bead are proportional to Cr(VI) binding affinity. This may be due to the weakening of the electrostatic interaction that results in the GO bond formation. These results show that the beads can be successfully regenerated and used at least six times for Cr(VI) adsorption.

Conclusions

The successful synthesis of novel MCSCl–GO composites for Cr(VI) adsorption was carried out. Adsorption was found to be optimum at pH 2 and at 25 °C. The composites followed the Langmuir isotherm indicating the adsorption mechanism is monolayer. Kinetic studies showed that adsorption of Cr(VI) on the composites follow a pseudo-second-order model, indicating that chemisorption is the rate-limiting step. Thermodynamic data revealed that the adsorption process was exothermic and spontaneous. The mechanism of adsorption occurs via ionic and electrostatic interactions between Cr(VI) ions and the composites. Rapid adsorption time and regeneration of the beads make the materials suitable for water systems with constant flow. MCSCl–GO–MnO_2 outperformed the other composites because of its higher binding affinity and increased reaction

spontaneity. All composites are durable in extreme pH environments and are suitable for polluted water treatment, which include methods utilising packed column reactors, or general immersion in running river water while contained in a porous material.

Acknowledgements This work was funded by the National Research Foundation (NRF), South Africa (Grant #95799), and the Eskom TESP Programme (Grant #P677). Microscopy images were taken by the Microscopy and Microanalysis Unit (MMU) at the University of Kwa Zulu-Natal.

References

Aragay G, Pons J, Merkoçi A (2011) Recent trends in macro-, micro-, and nanomaterial-based tools and strategies for heavy-metal detection. Chem Rev 111:3433–3458. https://doi.org/10.1021/cr100383r

Azarmi F, Mironov E, Shakhova I, Safonov A (2018) Effect of Microstructural Characteristics on Thermal and Electrical Properties of Thermally Sprayed Ceramic Coatings. In: Proceedings of the 41st International Conference on Advanced Ceramics and Composites, vol 38. Wiley, pp 113–123. https://doi.org/10.1002/9781119474678.ch11

Azuaje J et al (2017) An efficient and recyclable 3D printed α-Al_2O_3 catalyst for the multicomponent assembly of bioactive heterocycles. Appl Catal A 530:203–210. https://doi.org/10.1016/j.apcata.2016.11.031

Barrera-Díaz CE, Lugo-Lugo V, Bilyeu B (2012) A review of chemical, electrochemical and biological methods for aqueous Cr(VI) reduction. J Hazard Mater 223–224:1–12. https://doi.org/10.1016/j.jhazmat.2012.04.054

Belgin Ergül NB, Mehmet SÖ (2014) The use of manganese oxide minerals for the removal arsenic and selenium anions from aqueous solutions. Energy Environ Eng 2:103–112. https://doi.org/10.13189/eee.2014.020501

Chen S, Zhu J, Wu X, Han Q, Wang X (2010) Graphene oxide – MnO_2 nanocomposites for supercapacitors. ACS Nano 4:2822–2830. https://doi.org/10.1021/nn901311t

Costa M (1997) Toxicity and carcinogenicity of Cr(VI) in animal models and humans. Crit Rev Toxicol 27:431–442. https://doi.org/10.3109/10408449709078442

Devaraj S, Munichandraiah N (2008) Surfactant stabilized nanopetals morphology of α-MnO_2 prepared by microemulsion method. J Solid State Electrochem 12:207–211

Donadel K, Felisberto MD, Fávere VT, Rigoni M, Batistela NJ, Laranjeira MC (2008) Synthesis and characterization of the iron oxide magnetic particles coated with chitosan biopolymer. Mater Sci Eng, C 28:509–514

Du Y, Wang L, Wang J, Zheng G, Wu J, Dai H (2015) Flower-, wire-, and sheet-like MnO_2-deposited diatomites: highly efficient absorbents for the removal of Cr(VI). J Environ Sci 29:71–81. https://doi.org/10.1016/j.jes.2014.06.047

Elwakeel KZ (2009) Removal of reactive black 5 from aqueous solutions using magnetic chitosan resins. J Hazard Mater 167:383–392

Fan L, Luo C, Sun M, Li X, Lu F, Qiu H (2012a) Preparation of novel magnetic chitosan/graphene oxide composite as effective adsorbents toward methylene blue. Bioresour Technol 114:703–706. https://doi.org/10.1016/j.biortech.2012.02.067

Fan Y, Jiang W, Kawasaki A (2012b) Highly conductive few-layer graphene/Al_2O_3 nanocomposites with tunable charge carrier type. Adv Funct Mater 22:3882–3889. https://doi.org/10.1002/adfm.201200632

Ge J, Deng K, Cai W, Yu J, Liu X, Zhou J (2013) Effect of structure-directing agents on facile hydrothermal preparation of hierarchical γ-Al_2O_3 and their adsorption performance toward Cr(VI) and CO_2. J Colloid Interface Sci 401:34–39. https://doi.org/10.1016/j.jcis.2013.03.028

Gheju M, Balcu I, Mosoarca G (2016) Removal of Cr(VI) from aqueous solutions by adsorption on MnO_2. J Hazard Mater 310:270–277. https://doi.org/10.1016/j.jhazmat.2016.02.042

Glisoni RJ, Molina M, Calderón M, Moglioni AG, Sosnik A (2015) Chitosan-g-oligo (epsilon-caprolactone) polymeric micelles: microwave-assisted synthesis and physicochemical and cytocompatibility characterization. J Mater Chem B 3:4853–4864

Gupta VK, Gupta M, Sharma S (2001) Process development for the removal of lead and chromium from aqueous solutions using red mud—an aluminium industry waste. Water Res 35:1125–1134. https://doi.org/10.1016/S0043-1354(00)00389-4

Haeri SZ, Ramezanzadeh B, Asghari M (2017) A novel fabrication of a high performance SiO_2-graphene oxide (GO) nanohybrids: characterization of thermal properties of epoxy nanocomposites filled with SiO_2-GO nanohybrids. J Colloid Interface Sci 493:111–122. https://doi.org/10.1016/j.jcis.2017.01.016

Han G, Liu Y, Kan E, Tang J, Zhang L, Wang H, Tang W (2014) Sandwich-structured MnO_2/polypyrrole/reduced graphene oxide hybrid composites for high-performance supercapacitors. RSC Adv 4:9898–9904

Hu X-j et al (2011) Adsorption of chromium (VI) by ethylenediamine-modified cross-linked magnetic chitosan resin: isotherms, kinetics and thermodynamics. J Hazard Mater 185:306–314

Huang G, Yang C, Zhang K, Shi J (2009) Adsorptive removal of copper ions from aqueous solution using cross-linked magnetic chitosan beads. Chin J Chem Eng 17:960–966. https://doi.org/10.1016/S1004-9541(08)60303-1

Hummers WS Jr, Offeman RE (1958) Preparation of graphitic oxide. J Am Chem Soc 80:1339–1339

Jastrzębska A et al (2016) Synthesis of the RGO/Al_2O_3 core–shell nanocomposite flakes and characterization of their unique electrostatic properties using zeta potential measurements. Appl Surf Sci 362:577–594

Jiang H, Yang L, Li C, Yan C, Lee PS, Ma J (2011) High-rate electrochemical capacitors from highly graphitic carbon-tipped manganese oxide/mesoporous carbon/manganese oxide hybrid nanowires. Energy Environ Sci 4:1813–1819. https://doi.org/10.1039/C1EE01032H

Jodeh S et al (2016) Using thiophene supported on SiO_2 for removal Cr(VI) from water receptor. Appl J Envir Eng Sci 2:78–94

Karthikeyan T, Rajgopal S, Miranda LR (2005) Chromium(VI) adsorption from aqueous solution by Hevea Brasilinesis sawdust activated carbon. J Hazard Mater 124:192–199. https://doi.org/10.1016/j.jhazmat.2005.05.003

Kim BC, Park SW (2008) Fracture toughness of the nano-particle reinforced epoxy composite. Compos Struct 86:69–77

Kim M, Hwang Y, Kim J (2013) Graphene/MnO_2-based composites reduced via different chemical agents for supercapacitors. J Power Sources 239:225–233

Kou L, Gao C (2011) Making silica nanoparticle-covered graphene oxide nanohybrids as general building blocks for large-area superhydrophilic coatings. Nanoscale 3:519–528

Kul AR, Koyuncu H (2010) Adsorption of Pb(II) ions from aqueous solution by native and activated bentonite: kinetic, equilibrium and thermodynamic study. J Hazard Mater 179:332–339. https://doi.org/10.1016/j.jhazmat.2010.03.009

Kumar S, Koh J (2014) Physiochemical and optical properties of chitosan based graphene oxide bionanocomposite. Int J

Biol Macromol 70:559–564. https://doi.org/10.1016/j.ijbiomac.2014.07.019
Kurniawan TA, Chan GYS, Lo W-H, Babel S (2006) Physico–chemical treatment techniques for wastewater laden with heavy metals. Chem Eng J 118:83–98. https://doi.org/10.1016/j.cej.2006.01.015
Kyzas GZ, Kostoglou M, Lazaridis NK (2009) Copper and chromium(VI) removal by chitosan derivatives—equilibrium and kinetic studies. Chem Eng J 152:440–448. https://doi.org/10.1016/j.cej.2009.05.005
Lee H, Jeong Y, Min B, Lyoo W, Lee S (2009) Preparation and acid dye adsorption behavior of polyurethane/chitosan composite foams. Fibers Polym 10:636–642. https://doi.org/10.1007/s12221-010-0636-1
Li J, Zhang S, Chen C, Zhao G, Yang X, Li J, Wang X (2012) Removal of Cu(II) and fulvic acid by graphene oxide nanosheets decorated with Fe_3O_4 nanoparticles ACS. Appl Mater Interfaces 4:4991–5000. https://doi.org/10.1021/am301358b
Lin S, Kiang C (2003) Chromic acid recovery from waste acid solution by an ion exchange process: equilibrium and column ion exchange modeling. Chem Eng J 92:193–199
Liu L, Li C, Bao C, Jia Q, Xiao P, Liu X, Zhang Q (2012) Preparation and characterization of chitosan/graphene oxide composites for the adsorption of Au(III) and Pd(II). Talanta 93:350–357. https://doi.org/10.1016/j.talanta.2012.02.051
Liu M, Wen T, Wu X, Chen C, Hu J, Li J, Wang X (2013) Synthesis of porous Fe_3O_4 hollow microspheres/graphene oxide composite for Cr(VI) removal. Dalton Trans 42:14710–14717. https://doi.org/10.1039/c3dt50955a
Lu W, Luo Y, Chang G, Sun X (2011) Synthesis of functional SiO_2-coated graphene oxide nanosheets decorated with Ag nanoparticles for H_2O_2 and glucose detection. Biosens Bioelectron 26:4791–4797. https://doi.org/10.1016/j.bios.2011.06.008
Luo X, Zeng J, Liu S, Zhang L (2015) An effective and recyclable adsorbent for the removal of heavy metal ions from aqueous system: magnetic chitosan/cellulose microspheres. Bioresour Technol 194:403–406
Ma W, Ya F-Q, Han M, Wang R (2007) Characteristics of equilibrium, kinetics studies for adsorption of fluoride on magnetic-chitosan particle. J Hazard Mater 143:296–302. https://doi.org/10.1016/j.jhazmat.2006.09.032
Maksin DD, Nastasović AB, Milutinović-Nikolić AD, Suručić LT, Sandić ZP, Hercigonja RV, Onjia AE (2012) Equilibrium and kinetics study on hexavalent chromium adsorption onto diethylene triamine grafted glycidyl methacrylate based copolymers. J Hazard Mater 209–210:99–110. https://doi.org/10.1016/j.jhazmat.2011.12.079
Martins AF, Bueno PV, Almeida EA, Rodrigues FH, Rubira AF, Muniz EC (2013) Characterization of *N*-trimethyl chitosan/alginate complexes and curcumin release. Int J Biol Macromol 57:174–184
Mckay G, Blair H, Findon A (1986) Sorption of metal ions by chitosan. In: Proc. Conf. Immobilisation of Ions by BiosorptionSoc. Chem. Ind., Lancaster University
Mourya VK, Inamdar NN (2008) Trimethyl chitosan and its applications in drug delivery. J Mater Sci 20:1057. https://doi.org/10.1007/s10856-008-3659-z
Ozaki H, Sharma K, Saktaywin W (2002) Performance of an ultra-low-pressure reverse osmosis membrane (ULPROM) for separating heavy metal: effects of interference parameters. Desalination 144:287–294. https://doi.org/10.1016/S0011-9164(02)00329-6
Palimi M, Rostami M, Mahdavian M, Ramezanzadeh B (2014) Application of EIS and salt spray tests for investigation of the anticorrosion properties of polyurethane-based nanocomposites containing Cr_2O_3 nanoparticles modified with 3-amino propyl trimethoxy silane. Prog Org Coat 77:1935–1945
Pugazhenthi G, Sachan S, Kishore N, Kumar A (2005) Separation of chromium (VI) using modified ultrafiltration charged carbon membrane and its mathematical modeling. J Membr Sci 254:229–239
Rozenberg BA, Tenne R (2008) Polymer-assisted fabrication of nanoparticles and nanocomposites. Prog Polym Sci 33:40–112. https://doi.org/10.1016/j.progpolymsci.2007.07.004
Sekine T, Nakatani K (2002) Intraparticle diffusion and adsorption isotherm for sorption in silica gel studied by single-microparticle injection and microabsorption methods. Langmuir 18:694–697. https://doi.org/10.1021/la0110500
Sharma YC, Srivastava V, Mukherjee AK (2010) Synthesis and application of nano-Al_2O_3 powder for the reclamation of hexavalent chromium from aqueous solutions. J Chem Eng Data 55:2390–2398. https://doi.org/10.1021/je900822j
Shaygan M, Davami K, Kheirabi N, Baek CK, Cuniberti G, Meyyappan M, Lee J-S (2014) Single-crystalline CdTe nanowire field effect transistors as nanowire-based photodetector. Phys Chem Chem Phys 16:22687–22693. https://doi.org/10.1039/C4CP03322A
Sieval AB, Thanou M, Kotze AF, Verhoef JC, Brussee J, Junginger HE (1998) Preparation and NMR characterization of highly substituted *N*-trimethyl chitosan chloride. Carbohydr Polym 36:157–165. https://doi.org/10.1016/S0144-8617(98)00009-5
Sun X, Yang L, Li Q, Zhao J, Li X, Wang X, Liu H (2014) Amino-functionalized magnetic cellulose nanocomposite as adsorbent for removal of Cr(VI): synthesis and adsorption studies. Chem Eng J 241:175–183. https://doi.org/10.1016/j.cej.2013.12.051
Tamura H, Katayama N, Furuichi R (1997) The Co^{2+} adsorption properties of Al_2O_3, Fe_2O_3, Fe_3O_4, TiO_2, and MnO_2 evaluated by modeling with the frumkin isotherm. J Colloid Interface Sci 195:192–202
Thinh NN et al (2013) Magnetic chitosan nanoparticles for removal of Cr(VI) from aqueous solution. Mater Sci Eng, C 33:1214–1218. https://doi.org/10.1016/j.msec.2012.12.013
Tiwari I, Singh M, Pandey CM, Sumana G (2015) Electrochemical genosensor based on graphene oxide modified iron oxide–chitosan hybrid nanocomposite for pathogen detection. Sens Actuators, B 206:276–283. https://doi.org/10.1016/j.snb.2014.09.056
Wan M-W, Kan C-C, Rogel BD, Dalida MLP (2010) Adsorption of copper (II) and lead (II) ions from aqueous solution on chitosan-coated sand. Carbohydr Polym 80:891–899. https://doi.org/10.1016/j.carbpol.2009.12.048
Weber W, Morris J (1962) Removal of biologically-resistant pollutants from waste waters by adsorption. Adv Water Pollut Res 2:231–266
Wu Y, Luo H, Wang H, Wang C, Zhang J, Zhang Z (2013) Adsorption of hexavalent chromium from aqueous solutions by graphene modified with cetyltrimethylammonium bromide. J Colloid Interface Sci 394:183–191. https://doi.org/10.1016/j.jcis.2012.11.049
Yang S et al (2015) Preparation of graphene oxide decorated Fe_3O_4@SiO_2 nanocomposites with superior adsorption capacity and SERS detection for organic dyes. J Nanomater 16:337
Yu Z, Di H, Ma Y, Lv L, Pan Y, Zhang C, He Y (2015) Fabrication of graphene oxide–alumina hybrids to reinforce the anti-corrosion performance of composite epoxy coatings. Appl Surf Sci 351:986–996
Zhou F, Zhao X, Yuan C, Xu H (2007) Synthesis of γ-MnOOH nanorods and their isomorphous transformation into β-MnO_2 and α-Mn_2O_3 nanorods. J Mater Sci 42:9978–9982
Zhu J et al (2012) One-pot synthesis of magnetic graphene nanocomposites decorated with core@double-shell nanoparticles for fast chromium removal. Environ Sci Technol 46:977–985. https://doi.org/10.1021/es2014133

Publisher's Note